Binding site programmable self-assembly of 3D hierarchical DNA origami nanostructures

Xingfei Wei,[†,‖] Chi Chen,[‡,‖] Alexander Popov,[†] Mark Bathe,[*,‡] and Rigoberto Hernandez[*,†,¶,§]

†*Department of Chemistry, Johns Hopkins University, Baltimore, Maryland 21218, USA*

‡*Department of Biological Engineering, Massachusetts Institute of Technology, Cambridge, Massachusetts 02139, United States*

¶*Department of Chemical & Biomolecular Engineering, Johns Hopkins University, Baltimore, Maryland 21218, USA*

§*Department of Materials Science and Engineering, Johns Hopkins University, Baltimore, Maryland 21218, USA*

‖*Contributed equally to this work*

E-mail: mbathe@mit.edu; r.hernandez@jhu.edu

Abstract

DNA nanotechnology has broad applications in biomedical drug delivery and programmable materials. Characterization of the self-assembly of DNA origami and quantum dots (QDs) is necessary for the development of new DNA-based nanostructures. We use computation and experiment to show that the self-assembly of 3D hierarchical nanostructures can be controlled by programming the binding site number and their positions on DNA origami. Using biotinylated pentagonal pyramid wireframe DNA origamis and streptavidin capped QDs, we demonstrate that DNA origami with

1 binding site at the outer vertex can assemble multi-meric origamis with up to 6 DNA origamis on 1 QD, and DNA origami with 1 binding site at the inner center can only assemble monomeric and dimeric origamis. Meanwhile, the yield percentages of different multi-meric origamis are controlled by the QD:DNA-origami stoichiometric mixing ratio. DNA origamis with 2 binding sites at the $\alpha\gamma$ positions (of the pentagon) make larger nanostructures than those with binding sites at the $\alpha\beta$ positions. In general, increasing the number of binding sites leads to increases in the nanostructure size. At high DNA origami concentration, the QD number in each cluster becomes the limiting factor for the growth of nanostructures. We find that reducing the QD size can also affect the self-assembly because of the reduced access to the binding sites from more densely packed origamis.

1 Introduction

Hierarchical nanostructures of DNA and nanoparticles play an important role in biological sensing,[1–3] drug delivery,[1,3,4] programmable materials,[5–12] and computing materials.[8,13] Semi-conductive nanoparticles are uniquely important for advanced optical devices[7,14,15] and atmospheric chemistry.[16,17] Nature adopts self-assembly approaches to make large and complex biological systems, and this strategy has also proven to be important in fabricating functional materials and structures.[18] Using DNA nanotechnology, Seeman made such self-assembly programmable in 1982.[19] DNA origami capable of folding into arbitrary 2D patterns for extended, infinite systems was invented by Rothemund in 2006,[20] and later shown to be capable of designing 3D nanostructures for finite assemblies in 2009.[21] They were generalized to arbitrary wireframe assemblies such as nanobricks by the Bathe[22,23] and Högberg[24,25] labs. Such structures allow for DNA programmed nanoparticle assembly of core-satellite colloidal nanostructures demonstrated accurate and programmable control biological delivery;[26] gold nanoparticle (AuNP) mediated triangular shaped DNA origami assembly in plasmonics applications;[27] self-assembly of cesium lead halide 3D perovskite nanocrystals which exhibited super fluorescence;[28] and the possibility of solving maze for information processing using a DNA origami 2D platform.[29]

DNA coated nanoparticles (NPs)—e.g. AuNPs and quantum dots (QDs)—can self-assemble into 3D various colloidal crystals,[30] and the crystal structure can be regulated by the stoichiometric ratio of NP:DNA.[31] Emulsion droplets programmed by DNA can connect into polymer-like chains,[32] form colloidal foldamers with designed folding angles,[33] or carry multivalence with unique recognition in hierarchical nanostructures.[34] Protein 3D lattices were also assembled using DNA origami voxels.[35] Calcaterra et al.[36] showed that the process of colloidal crystal formation of DNA coated AuNPs first involves the aggregation of NPs into assemblies, and then their rearrangement into a crystal lattice. Large DNA coated AuNPs (10 nm in diameter) are programmable atom equivalents (PAEs) that can directly form colloidal crystals through PAE-PAE ionic bonding.[37,38] Meanwhile, small DNA coated AuNPs (2 nm in diameter) are electron equivalents (EEs) similar to electrons in metallic bonding that can stabilize the PAE lattice.[37,38] Controlling the valence number and valence position on NPs is the key to programming colloidal crystals. This has been realized using single-stranded DNA chains[39] and using DNA origami nanostructures.[35] Recently, various additional 2D and 3D hierarchical nanostructures have been assembled by DNA origami.[35,40–44] Using nano-focused hard x-ray tomography, Michelson et al.[42] achieved a 3D visualization of the diamond colloidal crystal lattice assembled by tetrahedral 2D DNA origami motifs. Chen et al.[44] developed a fast assembly technology to make 2D arrays of QDs with rhombic 2D DNA origami that reduces the fabrication time from days to minutes because of the use of a dehydration rehydration process. Their work demonstrated the power of DNA nanotechnology in fabricating nanoscale quantum rod assemblies, and offered a path towards scalable and low-cost micro light-emitting diode (microLED) device fabrication useful for augmented reality (AR) / virtual reality (VR) applications. As the control of the nanostructure is critical in all of these emerging applications, there remains significant promise for the discovery of techniques that allow for even greater flexibility and precision in nanofabrication.

In this work, we use computational models and experiments to demonstrate the self-assembly mechanism of pentagonal pyramid wireframe DNA origamis connected by QDs as a possible answer to this need. (For convenience, in the following text, we use the term, DNA origami, as a short-hand for pentagonal pyramid wireframe DNA origami.) The number and position of binding sites are programmed on the DNA origami. Although all-atom molecular dynamics (MD) simulations is capable of accurately calculating the structure of a DNA chain attached to a QD,[45,46] it is not able to simulate a large DNA origami nanostructure. Coarse-grained DNA models—e.g. the oxDNA model[47,48]—can simulate one DNA origami nanostructure, but can not simulate hundreds of DNA origamis. To simulate colloidal crystal self-assembling the Glotzer group developed the HOOMD-blue molecular dynamics and Monte Carlo package. With the help of this package, they found that the conformation entropy is very important in the self-assembly process.[49,50] However, its use entails extensive time dependent observations to reveal the mechanism and kinetics.[51] Therein lies the challenge in addressing the spatial-temporal behavior at the middle scales[52] of these systems with structural and dynamically self-consistent equations of motion.

Toward this end, in the present system of interest, we simulated the self-assembly process of DNA origami by coarse-graining the space and time at larger scales with models that have been vetted with experiment. Specifically, we developed a convenient colloidal DNA origami model that is capable of simulating clustering nanostructures using 500 building blocks (DNA origamis + QDs) at once; see Fig. 1. We further show below, that this model reproduces the self-assembly of these materials seen in experiment. In combination of simulation and experiment, we thus aim to demonstrate the conclusion that these materials can be programmed through the engineered placement of the binding sites on the DNA origamis. There is precedent for synthesizing tailorable macroscale architectures using nanoscale material building blocks.[53] Through the present work, we expand dramatically the number and variation of the building blocks available for the construction of long-lived stable materials with nanoscale precision.

2 Methods

2.1 Computational models and methods

Our MD simulations were propagated using the Large-scale Atomic Molecular Massively Parallel Simulator (LAMMPS) package.[54] We replicated the DNA origami and QD single structures to make 3 different mixing ratios, viz — 100 QDs + 400 DNA origamis, 250 QDs + 250 DNA origamis, and 400 QDs + 100 DNA origamis. The DNA origami and QD single structures were set as rigid bodies. Based on the precedent from computational and experimental references,[55–57] the biotin-SAv binding energy is between 18 and 40 kcal/mol. Consequently, we set the biotin and SAv interaction LJ energy constant to 25 kcal/mol. The NVT ensemble was used in all simulations at a temperature fixed by a Langevin thermostat to 300 K with the damping coefficient noted in the Supporting Information (SI). The resulting diffusion coefficient of DNA origami was found to be circa 116 μm^2/s, which matches the empirical prediction.[58] Typically, we first propagated the system with the biotin-SAv binding interaction turned off for 250 μs to distribute the QDs and DNA origamis randomly and uniformly within the periodic simulation box; see Fig. 1K. We then performed the production runs with the biotin-SAv binding interaction turned on. In general, each simulation is stopped at around 1500 μs when the final equilibrium is reached, or not long after 2000 μs which takes approximately 700 computing hours on 24 CPU cores. The total pairwise potential energy of each trajectory was recorded to check the self-assembly process; see SI for all such plots. We found that the model approaches equilibrium well within 2000 μs if the ratio of QD to DNA origami is 1:4. The reaction rate approached equilibrium slowly when the single binding site is at the inner center of the DNA origami. The numerical results were then fit to analytical reaction rate formula which provided rate constants useful for extrapolating to the equilibrium behavior.

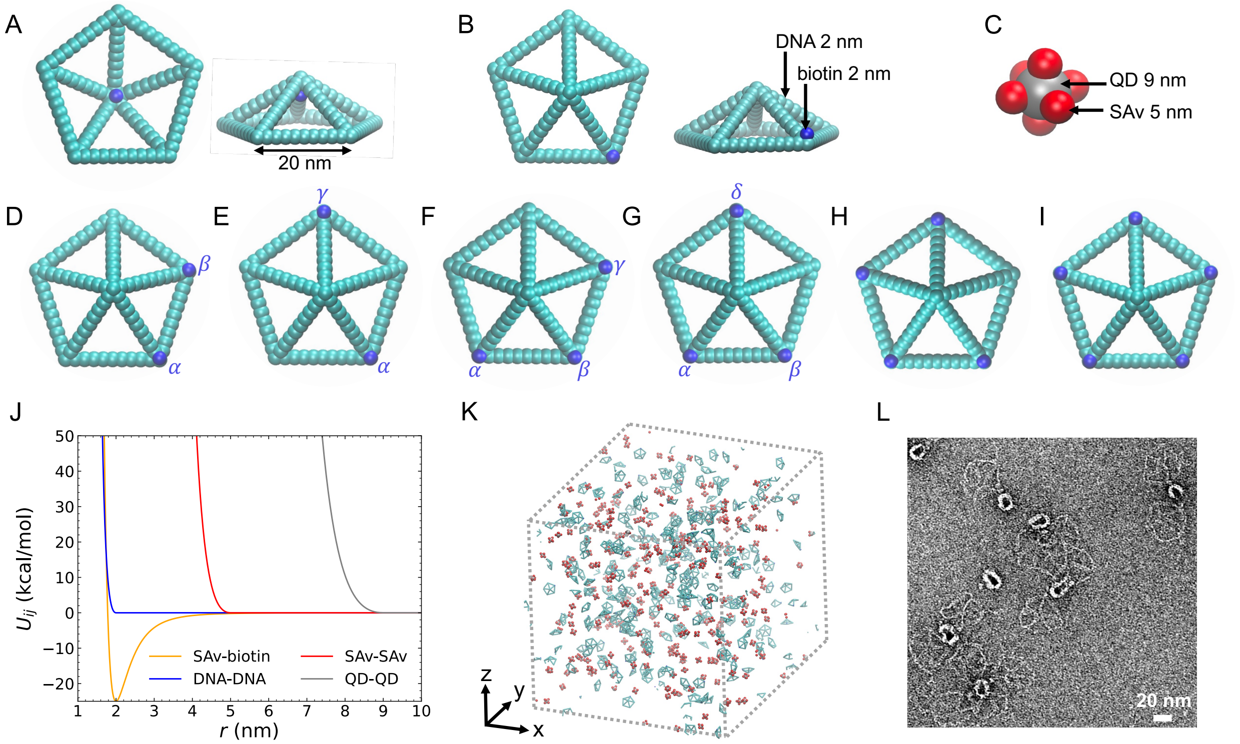

Figure 1: Computational and experimental visualizations of QD and origami components. Pentagonal pyramid DNA origami can be constructed with the biotin binding site at the inner center (A) or at the outer vertex (B). In all such structures, the edges are of equal length at 20 nm, and comprised of 10 DNA origami particles with 2 nm diameters (green). The biotin particle is also 2 nm in diameter (blue). The 9 nm diameter (gray) QD (C) is uniformly coated with 6 streptavidin (SAv) particles at 5 nm diameters (red). The biotin binding site numbers and positions on the DNA origami are programmed as following: 2 binding sites at $\alpha\beta$ positions (D), 2 binding sites at $\alpha\gamma$ positions (E), 3 binding sites at $\alpha\beta\gamma$ positions (F), 3 binding sites at $\alpha\beta\delta$ positions (G), 4 binding sites (H), and 5 binding sites (I). The biotin-SAv binding interaction (J) is described by a Lennard-Jones (LJ) potential, while other interactions are described by Weeks-Chandler-Andersen (WCA) potentials. A representative snapshot (K) of the initial trajectory (before assembly) shows the 250 QDs and 250 DNA origamis in the 600 nm × 600 nm × 600 nm simulation box (with periodic boundary conditions in 3 dimensions). A representative Transmission Electron Microscopy (TEM) image (L) of the clusters from QD:DNA-origami mixing ratio equals 1:1.

2.2 Experimental materials and methods

SAv capped QDs were purchased from Thermo Fisher Scientific. TAE buffers were purchased from Corning®. DNA oligonucleotides were purchased from Integrated DNA Technologies (IDT) and all DNA sequences are listed in Tables S2 and S3 in SI. $MgCl_2$ were purchased from Life Technologies Corporation DBA Invitrogen. The custom circular DNA scaffold pF1A were prepared according to previous work.[59] Pentagonal pyramid DNA origamis were folded in a solution of 15 nM scaffold (pF1A), 150 nM staples, 1×TAE, and 12 mM $MgCl_2$., then annealed over the course of 2 h on a Bio-Rad T100 thermocycler. Folded DNA origamis were purified by centrifugation and using an ultracentrifugal filter (Amicon 100 kDa). Five different configurations of binding positions on DNA origamis were constructed and analyzed: (1) 1 binding site at the inner center, (2) 1 binding site at the outer vertex, (3) 2 binding sites at the $\alpha\beta$ positions, (4) 2 binding sites at $\alpha\gamma$ positions, and (5) 5 binding sites at all corners on the pentagon. DNA origamis were incubated with QDs at room temperature overnight. Due to the biotin-SAv binding interaction, DNA origamis and QDs can self-assemble into nanostructures. Structural characterizations were carried out by ThermoFisher FEI Tecnai Spirit TEM at 120 kV. Dynamic Light Scattering (DLS) measurements were performed on a Malvern Zetasizer Ultra (Malvern Instruments) with three parallel measurements ($n = 3$). DLS frequency is calculated from the number (percentage).

3 Results and Discussion

3.1 Stoichiometrically Controlled Nanostructure Self-Assembly for 1 Binding Site on DNA origami

In the materials reported here, we took advantage of favorable biotin and SAv non-covalent interactions[60] to connect DNA origamis and QDs. This attraction was successfully leveraged earlier in making end-to-end connections between gold nano rods.[61] Our computational coarse-grained model has been benchmarked to experiment.[46] Each DNA origami is programmed through the attachment of 1 to 5 biotin binding sites at various positions, and QDs are coated with 6 SAv particles; see Fig. 1A-I. Each DNA origami or QD moves as a rigid body in the simulations. The biotin-SAv interaction is the only binding interaction, and it is described by a LJ potential with an energy constant of 25 kcal/mol. All other interactions are described by the WCA potential;[62] see the force field in Fig. 1J. The total number of DNA origami and QD in the model is 500, which corresponds to a total concentration of 3.85 μM. A representative scheme of 250 QDs + 250 DNA origamis is show in Fig. 1K. The colloidal DNA origami model structure is compared with the oxDNA model in Fig. S1 in SI. All force field parameters and simulation details are listed in Table S1 in SI. We also use experimental benchmarks to confirm the behavior observed in simulations of nanostructure assemblies as in, e.g., Fig. 1L.

The pentagonal pyramid DNA origami with 1 biotin binding site can be programmed at the inner center or the outer vertex; see Fig. 1A and B. When the binding site is at the outer vertex, the self-assembling products are a range of hetero-structures containing multiple origamis, which for simplicity we refer to as monomer, dimer, trimer, tetramer, pentamer, and hexamer when they contain the corresponding number of origamis. These multi-meric origamis are found in both simulation and experiment as shown in Fig. 2. Clark and coworkers[63] reported that 2D hierarchical assemblies of DNA origami dimer and multimer can be synthesized through their fluorous binding interaction. The reaction converting a monomer to a hexamer is a step-by-step process; see scheme Fig. 2A. A 2nd order reaction

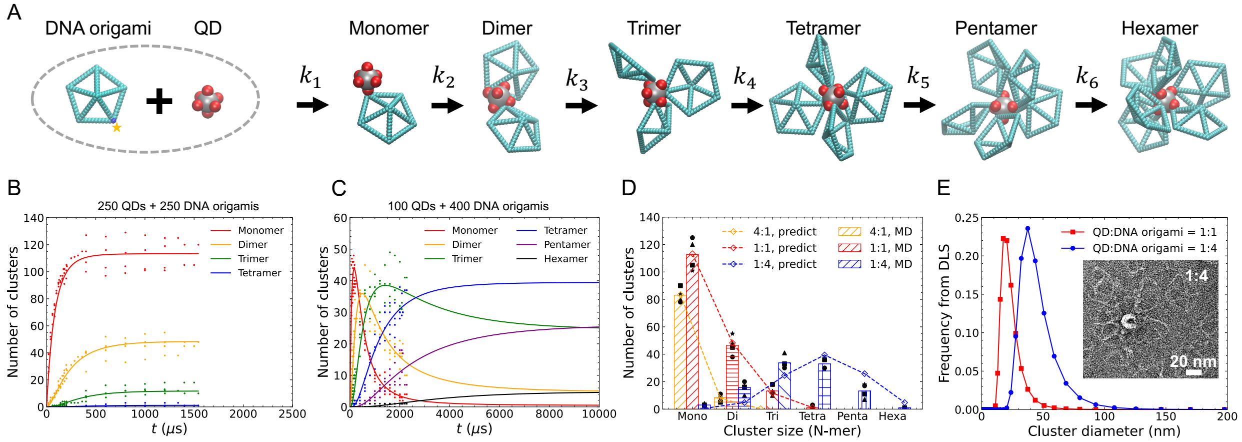

Figure 2: (A) Scheme of DNA origami self-assembly with QD when 1 biotin is bound at the outer vertex of the DNA origami in forming monomer, dimer, trimer, tetramer, pentamer, and hexamer hetero-structures step-by-step. (B) and (C) Time dependent numbers of different hetero-structures in the simulation box with 250 QDs and 250 DNA origamis, and with 100 QDs and 400 DNA origamis respectively. (D) Final products found at the end of simulation for 1 binding at outer vertex of DNA origami using different QD:DNA-origami mixing ratios. Four black dots in different symbols are from 4 different simulation trajectories; bars are averages of the 4 black dots. The colored symbols connected by dashed lines are the long-time limit of the fitted reaction kinetics (Eq. 1). (E) Comparison of DLS cluster size distribution measurement in experiment, for QD:DNA-origami mixing ratios at 1:1 vs 1:4. The DLS frequency is calculated from the number (percentage). The mean cluster diameters for the distributions shown here are 21.7 nm and 42.0 nm for QD:DNA-origami at 1:1 and 1:4, respectively. The inset shows a representative TEM image of a multi-mer at QD:DNA-origami equals 1:4. Dotted points in (B) and (C) are calculated from 4 different simulation trajectories; smooth curves are the result from a fit of the data points using Eq. 1. Additional observations are available in Figs. S2-S9 in SI, including cases when 1 biotin is bound on DNA origami at the inner center.

mechanism provided a good fit to our simulation results:

$$\begin{aligned}
\dot{N}_1 &= k_1 N_{\text{DNA}} \times N_{\text{QD}} - k_2 N_{\text{DNA}} \times N_1 \\
\dot{N}_2 &= k_2 N_{\text{DNA}} \times N_1 - k_3 N_{\text{DNA}} \times N_2 \\
\dot{N}_3 &= k_3 N_{\text{DNA}} \times N_2 - k_4 N_{\text{DNA}} \times N_3 \\
\dot{N}_4 &= k_4 N_{\text{DNA}} \times N_3 - k_5 N_{\text{DNA}} \times N_4 \\
\dot{N}_5 &= k_5 N_{\text{DNA}} \times N_4 - k_6 N_{\text{DNA}} \times N_5 \\
\dot{N}_6 &= k_6 N_{\text{DNA}} \times N_5 \\
\dot{N}_{\text{QD}} &= -k_1 N_{\text{DNA}} \times N_{\text{QD}} \\
\dot{N}_{\text{DNA}} &= -k_1 N_{\text{DNA}} \times N_{\text{QD}} - \sum k_{i-1} N_{\text{DNA}} \times N_i
\end{aligned} \tag{1}$$

where N_{DNA} is the number of DNA origamis, N_{QD} is the number of QDs, and N_i is that of the i-mers. The fitted curves in Figs. 2B and C are calculated using Eq. 1, allowing for the prediction of equilibrium beyond the computational time limit.

In our simulation model of 250 QDs and 250 DNA origamis, at a mixing ratio, QD:DNA-origami, equal to 1:1, monomers are the dominant products; see Fig. 2B. When the QD:DNA-origami mixing ratio increases to 1:4, tetramers become the dominant products; see Fig. 2C. Unfortunately, the simulation time (ca. 2000 μs) was not quite enough to fully reach this conclusion. Instead, the long-time behavior is obtained by fitting the analytic reaction rates in Eq. 1 over the simulation time and then extrapolating them to the long time limit. Consequently, the nanostructured products can be controlled stoichiometrically through the QD:DNA-origami mixing ratio. Fig. 2D compares the final cluster products among 3 different QD:DNA-origami mixing ratios. It shows that when these ratios change from 4:1 to 1:4, the dominant final products shift from monomers to tetramers; see also Figs. S3-S5 in the SI.

The effects from changing the QD:DNA-origami mixing ratio from 1:1 with 1:4 was also observed in experiments. We use DLS in Fig. 2E together with TEM images in Figs. S6 and S7 in SI to quantitatively and qualitatively compare cluster sizes at different mixing ratios. From DLS, we found that when the QD:DNA-origami ratio changes from 1:1 and 1:4, the mean hydrodynamic diameter and the peak positions of the clusters increase as noted in the caption. Since DNA origami is softer than the rigid structure assumed in the model,[46] it is not surprising that the hydrodynamic diameter measured in experiment is slightly smaller than that found in the models as indicated in Fig. 2A. Meanwhile, in both simulation and experiment, we found hexamers at the QD:DNA-origami ratio equal to 1:4. According to the reaction rates, the tetramer products will dominate, and the monomers will be entirely consumed at QD:DNA-origami equals 1:4. In the TEM images shown in Fig. S6 and S7 in SI, the monomers and tetramers are dominant at the QD:DNA-origami ratio equal to 1:1 and 1:4, respectively.

When the binding site is placed at the inner center of the DNA origami, the reaction rate is much slower. Therein, we found only monomers and dimers in the products; see Fig. S4 in SI. The dimer formed from an inner-center binding site is a closed structure with 2 DNA origamis capping the QD that prevents the binding of a third DNA origami. We also found that increasing the number of DNA origamis in the simulation to achieve a QD:DNA-origami ratio equal to 1:4 leads to an increased yield of dimers. However, increasing the QDs to a QD:DNA-origami ratio equal to 4:1 did not result in additional dimers. (See Fig. S8 in SI.) We found more dimer formation in the experiments (as shown in Fig. S9 in SI) than in the simulations,[46] largely because of the softness of the DNA origami is not fully described in the latter. The reaction rates from k_1 to k_6 decease quickly, when the number of DNA origamis binding to one QD increases; see Fig. S4 in SI. We found that the multi-mer nanostructure can be controlled by the stoichiometric ratio of QD:DNA-origami: Specifically, increasing the DNA origami concentration can increase the product nanostructure size. In literature, using the stoichiometric controlled method, it was also demonstrated that DNA-grafted nanoparticles can self-assemble into designed 3D crystal structures,[31] and DNA origamis can assemble into various designed 2D nanostructures.[41]

3.2 Position of the Binding Sites Affects their Structure and Behavior

The self-assembly of the nanostructure is spatially programmable. The DNA origamis are more likely to block each other when 2 biotin binding sites are next to each other at $\alpha\beta$ positions than if the biotin sites are at $\alpha\gamma$ positions; thus the structure can be programmed through the locations of the binding sites. Fig. 3A shows cluster size distribution histograms of DNA origamis and QDs in each cluster, at a mixing ratio of 250 DNA origamis to 250 QDs. The FS distribution (Eq. 2) is used to fit the cluster size distributions in Figs. 3A and F, which is based on the analogy between polymer size distributions in polymerization[64] and cluster growth:

$$p_x(N) = x^2 N (1-x)^{(N-1)} \tag{2}$$

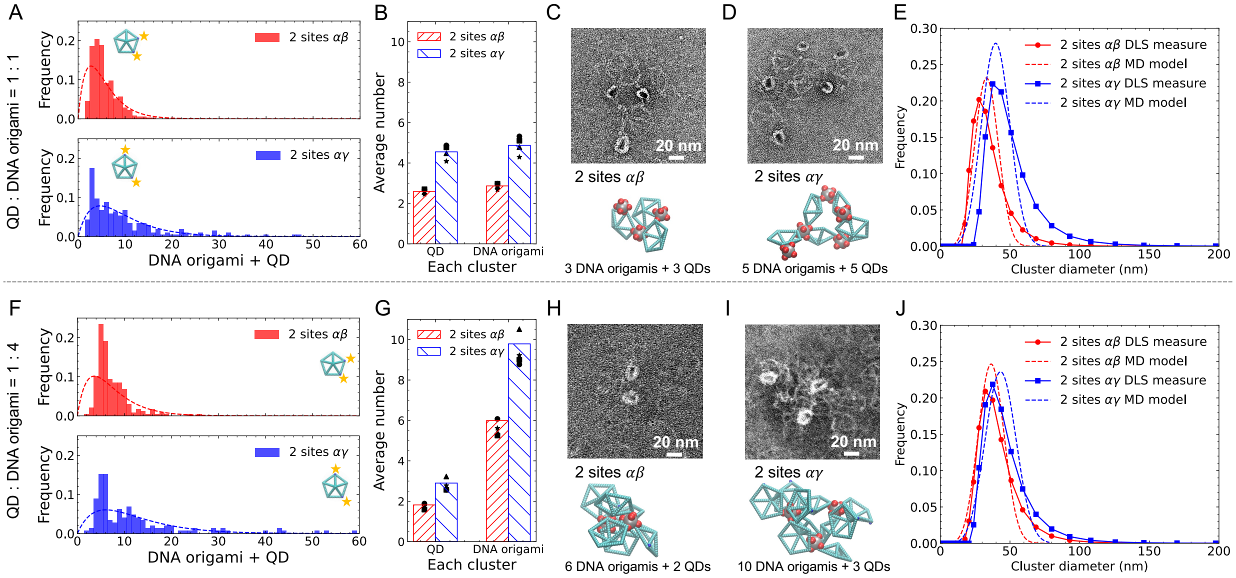

Figure 3: Comparing behavior resulting from origamis with binding sites at $\alpha\beta$ and $\alpha\gamma$ positions. The QD:DNA-origami mixing ratio is 1:1 in (A) - (E) and 1:4 in (F) - (J). (A) and (F) histograms of cluster size distributions obtained by counting the total number of DNA origamis plus QDs in each cluster. The dashed lines in (A) and (F) are fitted Flory-Schulz (FS) distributions using the same mean values as in the simulations. The total number of clusters we found in 4 different trajectories are 235, 145, 349, and 206 in (A) $\alpha\beta$ positions, (A) $\alpha\gamma$ positions, (F) $\alpha\beta$ positions, and (F) $\alpha\gamma$ positions, respectively. (B) and (G) give the average numbers of DNA origamis and QDs in each cluster from all simulations. (C), (D), (H) and (I) show representative cluster structures from experimental TEM images (upper) and simulation trajectories (lower). (E) and (J) compare experimental DLS of cluster size distributions in solid lines with model fits of the MD simulations in dashed lines. The MD model dashed lines in (E) and (J) are mapped from the fitted FS distribution in (A) and (F) using Eq. 3 , respectively. More detailed behavior arising from on DNA origamis with 2 bending sites at the $\alpha\beta$ and $\alpha\gamma$ positions is available in Figs. S10-S16 in SI.

where N is the number of DNA origamis or QDs in the cluster, x is a fitting parameter and $p_x(N)$ is the fraction of clusters with N DNA origamis or QDs. We set x to make the mean cluster size in the FS distribution match that in the MD simulation. To compare the FS distribution model fit with the DLS experimental measurements, we must include the Jacobian in the map of $p_x(N)$ (cluster size distribution based on the total number of DNA origamis and QDs) to $p(D)$ (cluster size distribution based on cluster diameter). That is,

$$p(D) = p_x(N)\frac{dN}{dD} \tag{3}$$

where $\frac{dN}{dD}$ is calculated from the derivative of the expression, $\frac{4\pi}{3}(\frac{D}{2})^3 = N\frac{4\pi}{3}(\frac{d}{2})^3$, between N and D. That latter equality is obtained by estimating the total volume of a cluster of diameter D to be equal to the sum of each DNA origami and QD whose diameter d is 20 nm.

The DNA origami and QD number distributions are provided separately in Fig. S11 in the SI. We found that the distributions from origamis with 2 binding sites $\alpha\gamma$ exhibit very large sized clusters, and the average cluster size from the origamis with binding sites at $\alpha\gamma$ is larger than those from $\alpha\beta$ positions; see Fig. 3B. Using a QD:DNA-origami ratio set at 1:1 in simulations, we found that origamis with 2 binding sites at the $\alpha\beta$ positions lead to an average cluster with 3 DNA origamis and 3 QDs, and origamis with 2 binding sites at the $\alpha\gamma$ positions lead to an average cluster with 5 DNA origamis and 5 QDs. We also found that the largest cluster contains 27 DNA origamis and 20 QDs for origamis with 2 biotin binding sites at the $\alpha\gamma$ positions, and it contains only 9 DNA origamis and 7 QDs for origamis with 2 biotin binding sites at the $\alpha\beta$ positions; see Fig. S12 in SI. The total pairwise binding potential energy for origamis with 2 binding sites at the $\alpha\beta$ and $\alpha\gamma$ positions are seen to be the same in Figs. S10 and S11 in SI. This result indicates that the total number of biotin-SAv pairs are also the same. We can deduce that when both the average cluster size of origamis with 2 binding sites at $\alpha\gamma$ is larger than those for the $\alpha\beta$ positions, and the total numbers of binding pairs are the same, then the total number of clusters of origamis with 2 binding sites $\alpha\gamma$ is less than that for the $\alpha\beta$ positions; see Fig. S11 in SI. The corresponding experimental TEM images and computational models are shown in Figs. 3C and D. The DLS results confirm the propensity for larger clusters from origamis with binding sites at the $\alpha\gamma$ positions; see Figs. 3E.

When the mixing ratio, QD:DNA-origami, changes to 1:4 in the simulations, we found that the DNA origami number distributions for origamis with binding sites at either the $\alpha\beta$ or $\alpha\gamma$ positions lead to an increase in the cluster sizes; see Fig. 3F. The corresponding QD number distributions show fewer QDs in all clusters; see Fig. S11 in SI. We also found an average cluster size of 6 DNA origamis and 2 QDs for origamis with 2 binding sites at $\alpha\beta$, and an average cluster size of 10 DNA origamis and 3 QDs in each cluster for origamis at 2 binding sites $\alpha\gamma$; see Fig. 3G. The largest cluster for origamis with 2 binding sites at the $\alpha\beta$ and $\alpha\gamma$ positions contains 19 and 44 DNA origamis, respectively; see Fig. S12 in SI. It remains valid in this limit, we continue to see that origamis with binding sites at the $\alpha\gamma$ positions lead to the self-assembly of larger nanostructures than those for the $\alpha\beta$ positions. Representative experimental TEM images and computational models are show in Figs. 3H and I. Our DLS results also show that the cluster diameters for 2 binding sites $\alpha\gamma$ positions is larger than $\alpha\beta$ positions; see Figs. 3J. Meanwhile, the difference in cluster size at QD:DNA-origami ratio equals 1:4 is much less than 1:1; see experimental results.

3.3 Self-Assembly using 3, 4, and 5 Binding Sites on DNA origami

Increasing the number of binding sites from 3 to 5, we found that the DNA origami number distributions in all 4 models have large clusters with more than 20 DNA origamis at the QD:DNA-origami mixing ratio equal to 1:1; see Fig. 4A. We also found more than 20 QDs in large clusters as indicated in corresponding QD number distributions available in Fig. S18 (a) in SI. The largest nanostructures from DNA origami with 3 binding sites at the $\alpha\beta\gamma$ positions, 3 binding sites at the $\alpha\beta\delta$ positions, 4 binding sites, and 5 binding sites contains 33, 35, 40, and 53 DNA origamis, respectively; see Fig. S19 in SI. The average number of DNA origamis and QDs in each cluster are shown in Fig. 4B, which shows that at QD:DNA-origami equals 1:1, the number of DNA origamis and QDs in each cluster are also the same. Figure 4B also shows that the average cluster size increases with the number of binding site increasing, when the number of binding sites is less than 4. The 4 and 5 binding site models yield similar cluster size distributions, average DNA origamis numbers, and pairwise potential energies; see Fig. 4A and B, and Figs. S17 and S18 in SI. The 3 binding sites $\alpha\beta\gamma$ positions results in a model yielding slightly larger clusters than using $\alpha\beta\delta$ positions.

An increasing trend in the average cluster size is observed as follows: (2 binding sites $\alpha\beta$)

$<$ (2 binding sites $\alpha\gamma$) $<$ (3 binding sites $\alpha\beta\gamma$) $<$ (3 binding sites $\alpha\beta\delta$) $<$ (4 binding sites) $\sim$ (5 binding sites). Meanwhile, the corresponding average numbers of DNA origamis in each cluster are 2.9, 4.9, 5.8, 7.6, 8.7, and 8.7. Also, the corresponding average numbers of QDs in each cluster are 2.6, 4.6, 5.6, 7.4, 8.7, and 8.7. Representative simulation structures for 4 different DNA origami models are shown in Fig. 4C. Representative TEM images and DLS cluster-size frequencies for 5 binding sites DNA origami are shown in Fig. 4D.

Meanwhile, increasing the QD:DNA-origami mixing ratio to 1:4 also changes the nanostructures, because the number of QDs limits the cluster growth; see Fig. 4E and F. Comparing with the results for the QD:DNA-origami mixing ratio equal to 1:1, the most pronounced distinction is that on average only 3 QDs are found for all nanostructures at the QD:DNA origami ratio equal to 1:4; see representative simulation behavior in Fig. 4G. The experimental DLS cluster-size frequencies and TEM images are shown in Fig. 4H. The DLS results confirm that for DNA origami models with 5 binding sites, the average cluster size at QD:DNA-origami equals 1:4 is much smaller than 1:1, see Fig. S18 (d) in SI. We also observe that the origamis with 3 binding sites at the $\alpha\beta\gamma$ positions yield slightly larger clusters than those at the $\alpha\beta\delta$ positions. At the QD:DNA-origami mixing ratio equal to 1:4, the total pairwise potential energies and the total number of clusters assembled are very similar across the 4 different DNA origami models with 3-5 binding sites; see Figs. S17 and S18 in SI. The size of the largest nanostructures found in simulations are very similar in 4 different models with 3-5 binding sites, and they all contain 34-39 DNA origamis and 11-13 QDs; see Figs. S19 in SI. At the QD:DNA-origami ratio equal to 1:4, the cluster size is limited by the QD concentration in solution, which reduces the QD number in each cluster. It turns out that increasing the number of binding sites on DNA origami does not affect the nanostructure size if the QD number is low; see Fig. S18 (h) in SI.

3.4 Variation in QD Size Leads to Varying Nanostructure

The QDs reported up to here were made with the same diameter equal to 9 nm. There is reason to expect that varying their size will have an effect on the resulting hetero-structures. It may be tempting to posit that the faster diffusion rates of the smaller QDs will lead to different structures, but these systems would exhibit such kinetic control only if there are traps that somehow quench them into thermodynamically disfavored structures. Instead, the size of the origamis generally affect the stability of subsequent additions of origamis because of blocking effects as we confirm below.

For QDs interacting with DNA origamis containing only one binding site at an outer vertex, we find in Fig. 5A that relative to the error bars, with decreasing QD size, the number of monomers remains approximately equal, and the number of dimers increases marginally. This results because the larger QDs admit the possibility for the addition of more origamis and hence there is a slight relative depletion in the smaller QD hetero-structures. Moreover, the number of resulting trimers and tetramers increase within increasing QD size, and no tetramer is found for the small 5 nm QD clusters. Thus, the DNA origamis on smaller QDs increasingly block each other spatially, and thereby inhibit the formation of of larger hetero-structures.

For QDs interacting with DNA origamis containing 2 binding sites at the $\alpha\beta$ positions, the average cluster sizes are similar for 5 - 9 nm QDs as shown in Fig. 5B. In all of these cases, the resulting clusters tend to contain 3 DNA origamis and 3 QDs. When 2 binding sites on a DNA origami are next to each other at the $\alpha\beta$ positions, the DNA origamis will spatially block each other, limiting increases in the resulting cluster size, and suppressing the impact of the QD size. For QDs interacting with DNA origamis containing 2 binding sites at the $\alpha\gamma$ positions, we find in Fig. 5C that the 5 nm QDs can assemble into clusters slightly larger than 7 to 9 nm QDs. The resulting clusters now tend to contain 6 DNA origamis. When 2 binding sites on a DNA origami are far away from each other at the $\alpha\gamma$ positions, larger QDs will bring linked DNA origamis closer, but smaller QDs can accommodate linked DNA origamis that are farther from each other leading to larger clusters. Comparisons between representative nanostructures for differently sized QDs are shown in Fig. 5D. The difference in size between QDs with diameters at 5 to 9 nm is not large and the resulting nanostructure size differences are not significant. This suggests that small QDs with a smaller number of SAv may be needed for applications requiring a larger number of connections. But the fact remains that control of the number and position of the binding sites leads to varying structures predictably.

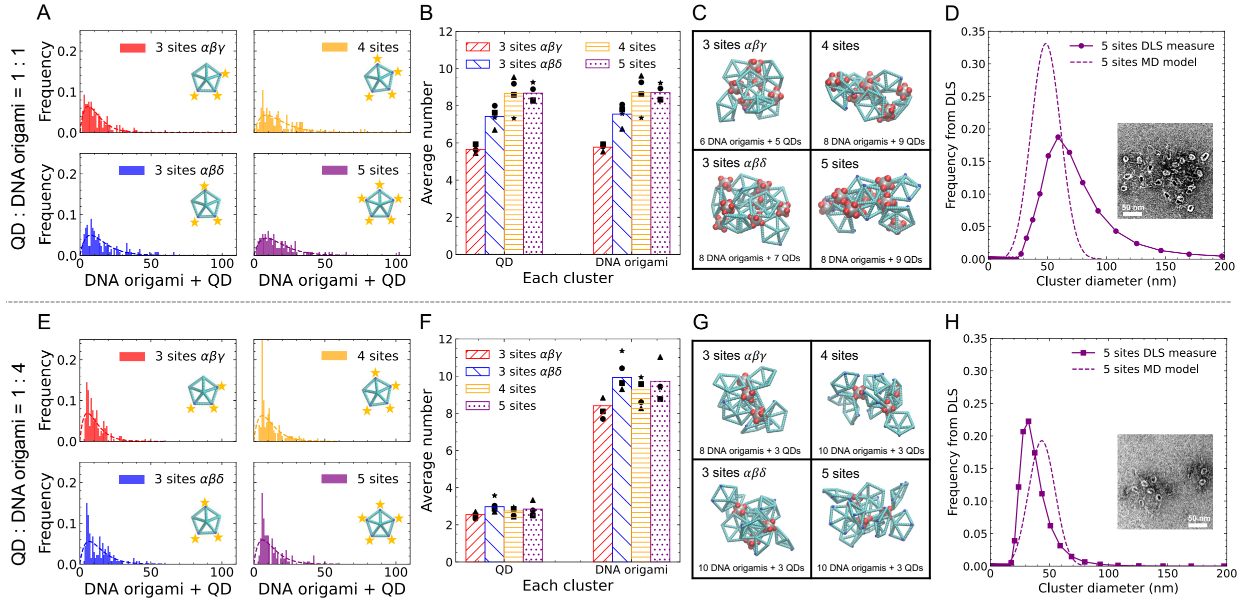

Figure 4: Comparison of resulting structures for DNA origami with 3 binding sites at the $\alpha\beta\gamma$ positions, 3 binding sites at the $\alpha\beta\delta$ positions, 4 binding sites, and 5 binding sites. The QD:DNA-origami mixing ratio is 1:1 in panels (A) - (D) and 1:4 in panels (E) - (H). The cluster size distributions in (A) and (E) are histograms counting the total number of DNA origamis plus QDs in each cluster. The dashed lines in (A) and (E) are the FS distributions fit to the corresponding mean values of the simulations. The total number of clusters in (A) are 160, 133, 150, and 143 resulting from origamis with 3 binding sites $\alpha\beta\gamma$, 3 binding sites $\alpha\beta\delta$, 4 binding sites, and 5 binding sites, respectively. The total number of clusters in (E) are 173, 133, 116, and 115 for these respective cases. (B) and (F): The average numbers of DNA origamis and QDs in each cluster from all simulations. (C) and (G): Representative nanostructures in simulations. (D) and (H): compare using 5 binding sites DNA origamis Cluster size distributions for DNA origamis with 5 binding sites obtained from the experimental DLS (solid curves) and from FS distribution fit to the simulation (dashed curves). The MD model curves (dashed) are mapped from the fits of the FS distribution using Eq. 3. The small panel in (D) and (H) show TEM images of representative nanostructures. More detailed behavior of DNA origamis with 3-5 binding sites is available in Figs. S17-S21 in SI.

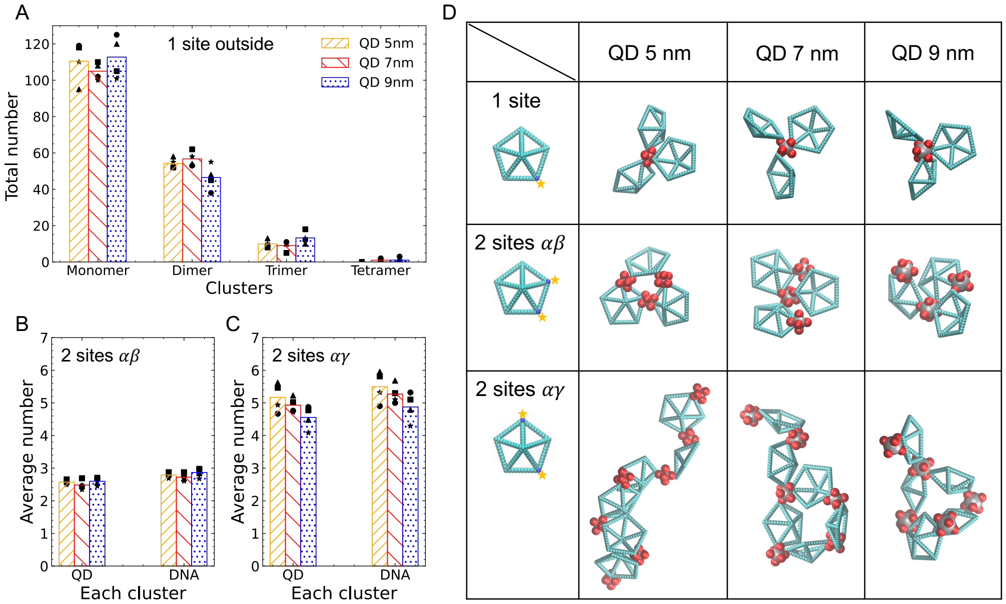

Figure 5: Simulations of QDs in different diameters at QD:DNA-origami mixing ratio of 1:1. (A) The total number of monomer, dimer, trimer, and tetramer found at the end of simulations using 1 binding site at the outer vertex of DNA origami. (B) The average number of DNA origami and QD in each cluster for 2 binding sites $\alpha\beta$ position on DNA origami. (C) The average number of DNA origami and QD in each cluster for 2 binding sites $\alpha\gamma$ position on DNA origami. (D) Representative nanostructures found in simulations for different QD sizes. For 5 nm and 7 nm QDs, only 1 long-time trajectory was simulated for each case. The total number of clusters found in each of the simulations is 88, 93, 42 and 44, for models with QD 5 nm + DNA origami 2 sites $\alpha\beta$, QD 7 nm + DNA origami 2 sites $\alpha\beta$, QD 5 nm + DNA origami 2 sites $\alpha\gamma$, and QD 7 nm + DNA origami 2 sites $\alpha\gamma$, respectively. (A), (B), and (C) share the same legend. Four black dots in different symbols are from 4 different simulation trajectories; bars are averages of the 4 black dots. Additional observations for different QD size effects are available in Figs. S22-S24 in SI.

4 Conclusions

We use computer simulations and experiments to show that by programming binding sites on the pentagonal pyramid wireframe DNA origami, we can control the self-assembly of DNA origamis with QDs. Origamis with only one binding site at the outer vertex can produce multi-mers containing 1 to 6 DNA origamis, while those with a binding site at the inner center can only produce monomers and dimers.

We calculate the reaction constants (k_1 to k_6) monomer to hexamer formation, and find that tuning the stoichiometric mixing ratio of QD:DNA-origami can control the multi-mer product distribution—e.g., for origamis with 1 binding site at the outer vertex, the monomer is the dominant product at a QD:DNA-origami ratio equal to 1:1 or higher, and the tetramer is the dominant product at a QD:DNA-origami ratio equal to 1:4. In both of the cases with 2 and 3 binding sites on DNA origamis, we found that when the binding sites are close to each other at the $\alpha\beta$ or $\alpha\beta\gamma$ positions, the nanostructure sizes are smaller than those resulting from the binding sites located at the $\alpha\gamma$ or $\alpha\beta\delta$ positions. We also found that increasing the number of binding sites to 4 or 5 yields similar nanostructure size distribution as 3 binding sites at the $\alpha\beta\delta$ positions. For origamis with multiple binding site DNA, the cluster structure is related to the stoichiometric mixing ratio of QD:DNA-origami. At a QD:DNA-origami ratio equal to 1:1, the average numbers of DNA origamis and QDs are also equal. At an overall QD:DNA-origami ratio equal to 1:4, the DNA origamis block each other from fully binding to the sites. The nanostructure size is consequently limited by the QD number and the resulting clusters have QD:DNA-origami ratios close to 1:3. Nevertheless, by changing the number of binding sites and the binding positions on DNA origami, we can synthesize nanostructures with self-limited size or make very large clusters. Thus our computational and experimental methods reveal the sensitivity of structure formation to the position and number of binding sites, and demonstrate that the binding sites on a DNA origami can be engineered to control the design of 3D hierarchical nanostructures.

Associated Content

The Supporting Information (SI) includes more information about computational and experimental methods, and additional results to support main figures.

Data Availability

The data that support the findings of this study are available from the corresponding author upon reasonable request.

Acknowledgments

This work has been partially supported by the National Science Foundation (NSF) through Grant No. CHE 2102455. Funding support to MB and CC from ONR N00014-21-1-4013 and NSF CCF 1956054 are gratefully acknowledged. The computing resources necessary for this work were performed in part on Expanse at the San Diego Supercomputing Center through allocation CTS090079 provided by Advanced Cyberinfrastructure Coordination Ecosystem: Services & Support (ACCESS), which is supported by National Science Foundation (NSF) grants #2138259, #2138286, #2138307, #2137603, and #2138296. Additional computing resources were provided by the Advanced Research Computing at Hopkins (ARCH) high-performance computing (HPC) facilities.

References

(1) Wang, P.; Meyer, T. A.; Pan, V.; Dutta, P. K.; Ke, Y. The Beauty and Utility of DNA Origami. *Chem* **2017**, *2*, 359–382, DOI: `10.1016/j.chempr.2017.02.009`.

(2) Engelen, W.; Dietz, H. Advancing Biophysics using DNA Origami. *Annu. Rev. Biophys.* **2021**, *50*, 469–492, DOI: `10.1146/annurev-biophys-110520-125739`.

(3) Knappe, G. A.; Wamhoff, E.-C.; Bathe, M. Functionalizing DNA Origami to Investigate and Interact with Biological Systems. *Nat. Rev. Mater.* **2023**, *8*, 123–138, DOI: `10.1038/s41578-022-00517-x`.

(4) Hu, Q.; Li, H.; Wang, L.; Gu, H.; Fan, C. DNA Nanotechnology-enabled Drug Delivery Systems. *Chem. Rev.* **2018**, *119*, 6459–6506, DOI: `10.1021/acs.chemrev.7b00663`.

(5) Jones, M. R.; Seeman, N. C.; Mirkin, C. A. Programmable Materials and the Nature of the DNA Bond. *Science* **2015**, *347*, 1260901, DOI: `10.1126/science.1260901`.

(6) Seeman, N. C.; Sleiman, H. F. DNA Nanotechnology. *Nat. Rev. Mater.* **2017**, *3*, 1–23, DOI: `10.1038/natrevmats.2017.68`.

(7) Hong, F.; Zhang, F.; Liu, Y.; Yan, H. DNA Origami: Scaffolds for Creating Higher Order Structures. *Chem. Rev.* **2017**, *117*, 12584–12640, DOI: `10.1021/acs.chemrev.6b00825`.

(8) Dey, S.; Fan, C.; Gothelf, K. V.; Li, J.; Lin, C.; Liu, L.; Liu, N.; Nijenhuis, M. A.; Saccà, B.; Simmel, F. C. et al. DNA Origami. *Nat. Rev. Methods Primers* **2021**, *1*, 13, DOI: `10.1038/s43586-020-00009-8`.

(9) Laramy, C. R.; O'Brien, M. N.; Mirkin, C. A. Crystal Engineering with DNA. *Nat. Rev. Mater.* **2019**, *4*, 201–224, DOI: `10.1038/s41578-019-0087-2`.

(10) Samanta, D.; Zhou, W.; Ebrahimi, S. B.; Petrosko, S. H.; Mirkin, C. A. Programmable Matter: the Nanoparticle Atom and DNA Bond. *Adv. Mater.* **2022**, *34*, 2107875, DOI: `10.1002/adma.202107875`.

(11) Kahn, J. S.; Gang, O. Designer Nanomaterials through Programmable Assembly. *Angew. Chem., Int. Ed.* **2022**, *134*, e202105678, DOI: `10.1002/ange.202105678`.

(12) Mirkin, C. A.; Petrosko, S. H. Inspired Beyond Nature: Three Decades of Spherical

Nucleic Acids and Colloidal Crystal Engineering with DNA. *ACS Nano* **2023**, *17*, 16291–16307, DOI: `10.1021/acsnano.3c06564`.

(13) Bathe, M.; Hernandez, R.; Komiyama, T.; Machiraju, R.; Neogi, S. Autonomous Computing Materials. *ACS Nano* **2021**, *15*, 3586–3592, DOI: `10.1021/acsnano.0c09556`.

(14) Madsen, M.; Gothelf, K. V. Chemistries for DNA Nanotechnology. *Chem. Rev.* **2019**, *119*, 6384–6458, DOI: `10.1021/acs.chemrev.8b00570`.

(15) García de Arquer, F. P.; Talapin, D. V.; Klimov, V. I.; Arakawa, Y.; Bayer, M.; Sargent, E. H. Semiconductor Quantum Dots: Technological Progress and Future Challenges. *Science* **2021**, *373*, eaaz8541, DOI: `10.1126/science.aaz8541`.

(16) Chen, H.; Nanayakkara, C. E.; Grassian, V. H. Titanium Dioxide Photocatalysis in Atmospheric Chemistry. *Chem. Rev.* **2012**, *112*, 5919–5948, DOI: `10.1021/cr3002092`.

(17) Nanayakkara, C. E.; Larish, W. A.; Grassian, V. H. Titanium Dioxide Nanoparticle Surface Reactivity with Atmospheric Gases, CO_2, SO_2 and NO_2: Roles of Surface Hydroxyl Groups and Adsorbed Water in the Formation and Stability of Adsorbed Products. *J. Phys. Chem. C* **2014**, *118*, 23011–23021, DOI: `10.1021/jp504402z`.

(18) Whitesides, G. M.; Grzybowski, B. Self-assembly at All Scales. *Science* **2002**, *295*, 2418–2421, DOI: `10.1126/science.1070821`.

(19) Seeman, N. C. Nucleic acid junctions and lattices. *J. Theor. Biol.* **1982**, *99*, 237–247, DOI: `10.1016/0022-5193(82)90002-9`.

(20) Rothemund, P. W. Folding DNA to Create Nanoscale Shapes and Patterns. *Nature* **2006**, *440*, 297–302, DOI: `10.1038/nature04586`.

(21) Douglas, S. M.; Dietz, H.; Liedl, T.; Högberg, B.; Graf, F.; Shih, W. M. Self-Assembly of DNA into Nanoscale Three-Dimensional Shapes. *Nature* **2009**, *459*, 414–418, DOI: `10.1038/nature08016`.

(22) Veneziano, R.; Ratanalert, S.; Zhang, K.; Zhang, F.; Yan, H.; Chiu, W.; Bathe, M. Designer Nanoscale DNA Assemblies Programmed from the Top Down. *Science* **2016**, *352*, 1534–1534, DOI: `10.1126/science.aaf4388`.

(23) Bathe, M.; Rothemund, P. W. DNA Nanotechnology: A Foundation for Programmable Nanoscale Materials. *MRS Bulletin* **2017**, *42*, 882–888, DOI: `10.1557/mrs.2017.279`.

(24) Benson, E.; Mohammed, A.; Gardell, J.; Masich, S.; Czeizler, E.; Orponen, P.; Högberg, B. DNA Rendering of Polyhedral Meshes at the Nanoscale. *Nature* **2015**, *523*, 441–444, DOI: `10.1038/nature14586`.

(25) Benson, E.; Mohammed, A.; Bosco, A.; Teixeira, A. I.; Orponen, P.; Högberg, B. Computer-Aided Production of Scaffolded DNA Nanostructures from Flat Sheet Meshes. *Angew. Chem., Int. Ed.* **2016**, *55*, 8869–8872, DOI: `10.1002/anie.201602446`.

(26) Chou, L. Y.; Zagorovsky, K.; Chan, W. C. DNA Assembly of Nanoparticle Superstructures for Controlled Biological Delivery and Elimination. *Nat. Nanotechnol.* **2014**, *9*, 148–155, DOI: `10.1038/nnano.2013.309`.

(27) Yao, G.; Li, J.; Chao, J.; Pei, H.; Liu, H.; Zhao, Y.; Shi, J.; Huang, Q.; Wang, L.; Huang, W. et al. Gold-Nanoparticle-Mediated Jigsaw-Puzzle-Like Assembly of Supersized Plasmonic DNA Origami. *Angew. Chem., Int. Ed.* **2015**, *54*, 2966–2969, DOI: `10.1002/anie.201410895`.

(28) Rainò, G.; Becker, M. A.; Bodnarchuk, M. I.; Mahrt, R. F.; Kovalenko, M. V.; Stöferle, T. Superfluorescence from Lead Halide Perovskite Quantum Dot Superlattices. *Nature* **2018**, *563*, 671–675, DOI: `10.1038/s41586-018-0683-0`.

(29) Chao, J.; Wang, J.; Wang, F.; Ouyang, X.; Kopperger, E.; Liu, H.; Li, Q.; Shi, J.; Wang, L.; Hu, J. et al. Solving Mazes with Single-Molecule DNA Navigators. *Nat. Mater.* **2019**, *18*, 273–279, DOI: `10.1038/s41563-018-0205-3`.

(30) Zhang, Y.; Lu, F.; Yager, K. G.; Van Der Lelie, D.; Gang, O. A General Strategy for the DNA-Mediated Self-Assembly of Functional Nanoparticles into Heterogeneous Systems. *Nat. Nanotechnol.* **2013**, *8*, 865–872, DOI: `10.1038/NNANO.2013.209`.

(31) Vo, T.; Venkatasubramanian, V.; Kumar, S.; Srinivasan, B.; Pal, S.; Zhang, Y.; Gang, O. Stoichiometric Control of DNA-Grafted Colloid Self-Assembly. *Proc. Natl. Acad. Sci. U.S.A.* **2015**, *112*, 4982–4987, DOI: `10.1073/pnas.1420907112`.

(32) Zhang, Y.; McMullen, A.; Pontani, L.-L.; He, X.; Sha, R.; Seeman, N. C.; Brujic, J.; Chaikin, P. M. Sequential Self-Assembly of DNA Functionalized Droplets. *Nat. Commun.* **2017**, *8*, 21, DOI: `10.1038/s41467-017-00070-0`.

(33) McMullen, A.; Muñoz Basagoiti, M.; Zeravcic, Z.; Brujic, J. Self-Assembly of Emulsion Droplets through Programmable Folding. *Nature* **2022**, *610*, 502–506, DOI: `10.1038/s41586-022-05198-8`.

(34) Zhang, Y.; He, X.; Zhuo, R.; Sha, R.; Brujic, J.; Seeman, N. C.; Chaikin, P. M. Multivalent, multiflavored droplets by design. *Proc. Natl. Acad. Sci. U.S.A.* **2018**, *115*, 9086–9091, DOI: `10.1073/pnas.1718511115`.

(35) Tian, Y.; Lhermitte, J. R.; Bai, L.; Vo, T.; Xin, H. L.; Li, H.; Li, R.; Fukuto, M.; Yager, K. G.; Kahn, J. S. et al. Ordered Three-Dimensional Nanomaterials using DNA-Prescribed and Valence-Controlled Material Voxels. *Nat. Mater.* **2020**, *19*, 789–796, DOI: `10.1038/s41563-019-0550-x`.

(36) Calcaterra, H. A.; Zheng, C. Y.; Seifert, S.; Yao, Y.; Jiang, Y.; Mirkin, C. A.; Deng, J.; Lee, B. Hints of Growth Mechanism Left in Supercrystals. *ACS Nano* **2023**, *17*, 15999–16007, DOI: `10.1021/acsnano.3c04365`.

(37) Girard, M.; Wang, S.; Du, J. S.; Das, A.; Huang, Z.; Dravid, V. P.; Lee, B.; Mirkin, C. A.; Olvera de la Cruz, M. Particle Analogs of Electrons in Colloidal Crystals. *Science* **2019**, *364*, 1174–1178, DOI: `10.1126/science.aaw8237`.

(38) Lee, S.; Calcaterra, H. A.; Lee, S.; Hadibrata, W.; Lee, B.; Oh, E.; Aydin, K.; Glotzer, S. C.; Mirkin, C. A. Shape Memory in Self-Adapting Colloidal Crystals. *Nature* **2022**, *610*, 674–679, DOI: `10.1038/s41586-022-05232-9`.

(39) Yao, G.; Li, J.; Li, Q.; Chen, X.; Liu, X.; Wang, F.; Qu, Z.; Ge, Z.; Narayanan, R. P.; Williams, D. et al. Programming Nanoparticle Valence Bonds with Single-Stranded Dna Encoders. *Nat. Mater.* **2020**, *19*, 781–788, DOI: `10.1038/s41563-019-0549-3`.

(40) Zhou, Y.; Dong, J.; Zhou, C.; Wang, Q. Finite Assembly of Three-Dimensional DNA Hierarchical Nanoarchitectures through Orthogonal and Directional Bonding. *Angew. Chem., Int. Ed.* **2022**, *134*, e202116416, DOI: `10.1002/ange.202116416`.

(41) Yin, J.; Xie, M.; Wang, J.; Cui, M.; Zhu, D.; Su, S.; Fan, C.; Chao, J.; Li, Q.; Wang, L. Gold-Nanoparticle-Mediated Assembly of High-Order DNA Nano-Architectures. *Small* **2022**, *18*, 2200824, DOI: `10.1002/smll.202200824`.

(42) Michelson, A.; Minevich, B.; Emamy, H.; Huang, X.; Chu, Y. S.; Yan, H.; Gang, O. Three-Dimensional Visualization of Nanoparticle Lattices and Multimaterial Frameworks. *Science* **2022**, *376*, 203–207, DOI: `10.1126/science.abk0463`.

(43) Dai, L.; Hu, X.; Ji, M.; Ma, N.; Xing, H.; Zhu, J.-J.; Min, Q.; Tian, Y. Programming the Morphology of DNA Origami Crystals by Magnesium Ion Strength. *Proc. Natl. Acad. Sci. U.S.A.* **2023**, *120*, e2302142120, DOI: `10.1073/pnas.2302142120`.

(44) Chen, C.; Luo, X.; Kaplan, A. E.; Bawendi, M. G.; Macfarlane, R. J.; Bathe, M. Ultrafast Dense DNA Functionalization of Quantum Dots and Rods for Scalable 2D Array Fabrication with Nanoscale Precision. *Sci. Adv.* **2023**, *9*, eadh8508, DOI: `10.1126/sciadv.adh8508`.

(45) Wei, X.; Chen, C.; Zhao, Y.; Harazinska, E.; Bathe, M.; Hernandez, R. Molecular Structure of Single-Stranded DNA on the ZnS Surface of Quantum Dots. *ACS Nano* **2022**, *16*, 6666–6675, DOI: `10.1021/acsnano.2c01178`.

(46) Chen, C.; Wei, X.; Parsons, M. F.; Guo, J.; Banal, J. L.; Zhao, Y.; Scott, M. N.; Schlau-Cohen, G. S.; Hernandez, R.; Bathe, M. Nanoscale 3D Spatial Addressing and Valence Control of Quantum Dots Using Wireframe DNA Origami. *Nat. Commun.* **2022**, *13*, 4935, DOI: `10.1038/s41467-022-32662-w`.

(47) Doye, J. P.; Fowler, H.; Prešern, D.; Bohlin, J.; Rovigatti, L.; Romano, F.; Šulc, P.; Wong, C. K.; Louis, A. A.; Schreck, J. S. et al. *DNA and RNA Origami: Methods and Protocols*; Springer, 2023; pp 93–112, DOI: `10.1007/978-1-0716-3028-0_6`.

(48) Wang, X.; Li, S.; Jun, H.; John, T.; Zhang, K.; Fowler, H.; Doye, J. P.; Chiu, W.; Bathe, M. Planar 2D Wireframe DNA Origami. *Sci. Adv.* **2022**, *8*, eabn0039, DOI: `10.1126/sciadv.abn0039`.

(49) Vo, T.; Glotzer, S. C. A Theory of Entropic Bonding. *Proc. Natl. Acad. Sci. U.S.A.* **2022**, *119*, e2116414119, DOI: `10.1073/pnas.2116414119`.

(50) Lee, S.; Vo, T.; Glotzer, S. C. Entropy Compartmentalization Stabilizes Open Host–Guest Colloidal Clathrates. *Nat. Chem.* **2023**, *15*, 905–912, DOI: `10.1038/s41557-023-01200-6`.

(51) Hensley, A.; Jacobs, W. M.; Rogers, W. B. Self-Assembly of Photonic Crystals by Controlling the Nucleation and Growth of DNA-Coated Colloids. *Proc. Natl. Acad. Sci. U.S.A.* **2022**, *119*, e2114050118, DOI: `10.1073/pnas.2114050118`.

(52) Clark, A. E.; Adams, H.; Hernandez, R.; Krylov, A. I.; Niklasson, A. M. N.; Sarupria, S.; Wang, Y.; Wild, S. M.; Yang, Q. The Middle Science: Traversing Scale in Complex Many-Body Systems. *ACS Cent. Sci.* **2021**, *7*, 1271, DOI: `10.1021/acscentsci.1c00685`.

(53) Macfarlane, R. J.; Lee, B.; Jones, M. R.; Harris, N.; Schatz, G. C.; Mirkin, C. A. Nanoparticle Superlattice Engineering with DNA. *Science* **2011**, *334*, 204–208, DOI: `10.1126/science.1210493`.

(54) Plimpton, S. J. Fast Parallel Algorithms for Short-Range Molecular Dynamics. *J. Comput. Phys.* **1995**, *117*, 1–19, DOI: `10.1006/jcph.1995.1039`.

(55) Li, Q.; Gusarov, S.; Evoy, S.; Kovalenko, A. Electronic Structure, Binding energy, and Solvation Structure of the Streptavidin-Biotin Supramolecular Complex: ONIOM and 3D-RISM Study. *J. Phys. Chem. B* **2009**, *113*, 9958–9967, DOI: `10.1021/jp902668c`.

(56) Miyamoto, S.; Kollman, P. A. Absolute and Relative Binding Free Energy Calculations of the Interaction of Biotin and Its Analogs with Streptavidin using Molecular Dynamics/Free Energy Perturbation Approaches. *Proteins: Struct., Func., Bioinf.* **1993**, *16*, 226–245, DOI: `10.1002/prot.340160303`.

(57) Liu, F.; Zhang, J. Z.; Mei, Y. The Origin of the Cooperativity in the Streptavidin-Biotin System: A Computational Investigation through Molecular Dynamics Simulations. *Sci. Rep.* **2016**, *6*, 27190, DOI: `10.1038/srep27190`.

(58) Robertson, R. M.; Laib, S.; Smith, D. E. Diffusion of Isolated DNA Molecules: Dependence on Length and Topology. *Proc. Natl. Acad. Sci. U.S.A.* **2006**, *103*, 7310–7314, DOI: `10.1073/pnas.0601903103`.

(59) Shepherd, T. R.; Du, R. R.; Huang, H.; Wamhoff, E.-C.; Bathe, M. Bioproduction of Pure, Kilobase-Scale single-stranded DNA. *Sci. Rep.* **2019**, *9*, 6121, DOI: `10.1038/s41598-019-42665-1`.

(60) Weber, P. C.; Ohlendorf, D. H.; Wendoloski, J.; Salemme, F. Structural Origins of High-Affinity Biotin Binding to Streptavidin. *Science* **1989**, *243*, 85–88, DOI: `10.1126/science.2911722`.

(61) Caswell, K.; Wilson, J. N.; Bunz, U. H.; Murphy, C. J. Preferential End-to-End Assembly of Gold Nanorods by Biotin-Streptavidin Connectors. *J. Am. Chem. Soc.* **2003**, *125*, 13914–13915, DOI: `10.1021/ja037969i`.

(62) Weeks, J. D.; Chandler, D.; Andersen, H. C. Role of Repulsive Forces in Determining the Equilibrium Structure of Simple Liquids. *J. Chem. Phys.* **1971**, *54*, 5237–5247, DOI: `10.1063/1.1674820`.

(63) Zou, J.; Stammers, A. C.; Taladriz-Sender, A.; Withers, J. M.; Christie, I.; Santana Vega, M.; Aekbote, B. L.; Peveler, W. J.; Rusling, D. A.; Burley, G. A. et al. Fluorous-directed assembly of DNA origami nanostructures. *ACS Nano* **2022**, *17*, 752–759, DOI: `10.1021/acsnano.2c10727`.

(64) Flory, P. J. Molecular Size Distribution in Linear Condensation Polymers. *J. Am. Chem. Soc.* **1936**, *58*, 1877–1885, DOI: `10.1021/ja01301a016`.

TOC Graphic